

University of Texas Rio Grande Valley

**ScholarWorks @ UTRGV**

---

Mechanical Engineering Faculty Publications  
and Presentations

College of Engineering and Computer Science

---

6-30-2022

## **Improved guidelines of indoor airborne transmission taking into account departure from the well-mixed assumption**

Jorge S. Salinas

K. A. Krishnaprasad

Nadim Zgheib

S. Balachandar





Follow this and additional works at: [https://scholarworks.utrgv.edu/me\\_fac](https://scholarworks.utrgv.edu/me_fac)



Part of the [Mechanical Engineering Commons](#)

---

## Improved guidelines of indoor airborne transmission taking into account departure from the well-mixed assumption

Jorge S. Salinas <sup>\*</sup>, K. A. Krishnaprasad , N. Zgheib , and S. Balachandar <sup>†</sup>  
*Department of Mechanical and Aerospace Engineering, University of Florida,  
Gainesville, Florida 32611, USA*



(Received 18 April 2022; accepted 14 June 2022; published 30 June 2022)

The well-mixed assumption has been widely used in predicting the spread of infectious diseases in indoor spaces. It is to be expected that a perfect well-mixed state will not be achieved in an indoor space at any reasonable level of ventilation. This work evaluates the well-mixed assumption by comparing the theory with results from large eddy simulations. The robustness of the well-mixed theory is established by comparing at four different levels. The comparison also points out systematic departures in pathogen concentration which can be accurately accounted for with an easily implementable correction factor to quantities such as cumulative exposure time. With the well-mixed model as the baseline, the correction factor can be used to account for additional important problem-specific details. We demonstrate that more accurately accounting for variability in pathogen concentration can help obtain improved estimates for enhanced guidelines of indoor airborne transmission. We further demonstrate that at source-sink separation distances smaller than 5 m, the well-mixed theory on average underestimates the risk of contagion, while for distances larger than about 5 m, the well-mixed theory's prediction, on average, is overly restrictive.

DOI: [10.1103/PhysRevFluids.7.064309](https://doi.org/10.1103/PhysRevFluids.7.064309)

### I. INTRODUCTION

The recent COVID-19 pandemic has devastated the lives and the livelihood of millions of people around the world. This devastation has brought increased awareness to the manner in which infectious diseases spread among the population. In particular, COVID-19 has now been well recognized to transmit from an infected person to a receiving host in three different ways: (i) *Direct route* of transmission where the ejected droplets, especially the larger ones, travel ballistically from the mouth or nose of the infected to the receiver. (ii) *Fomite route* of transmission where the droplets that fall to the ground or nearby surfaces are the source of contagion when the receiver comes into bodily contact with the infected surfaces. (iii) *Airborne route* of transmission where the ejected virus-laden small droplets quickly evaporate to become airborne nuclei that are carried by the air currents before infecting a receiving host [1–10]. The airborne route has been confirmed to be a potent mechanism of spreading since the airborne viruses can travel long distances before infecting scores of others. In fact, many of the documented super-spreading events from around the world have been connected with airborne transmission [8,11–16]. It should be noted however that in the few cases where direct contact or fomite transmission is presumed, respiratory transmission has not been completely excluded [17].

---

\*josalinas@ufl.edu

†bala1s@ufl.edu

The viruses are typically a hundred nanometers or smaller in size, and therefore they can be easily carried far and wide by airborne micron-sized nuclei that are not visible to the naked eye. The rich aroma of fresh brewed coffee or hot baked bread wafting through the air and reaching the far corners of a building provide ample evidence that airborne viruses can indeed travel long distances from their point of origin. This analogy also highlights the important difference between indoor and outdoor spreading of the virus-laden nuclei. In an indoor space, the average viral concentration, due to a continuous release of virus-laden nuclei by an infectious source, may reach a substantial level that could infect a number of occupants. This is why airborne transmission has been identified as the primary mode of infection in the super-spreading events mentioned above [8]. In contrast, in outdoor spaces, under most prevailing ambient conditions, the dilution of viral contagion is typically strong enough that the probability of spreading is greatly diminished [18].

The past two years have seen vigorous research toward quantifying the generation of virus-laden nuclei from breathing, talking, coughing, and sneezing [6,19–27] as well as the dispersal of airborne nuclei within indoor spaces to infect others [2,8,28–35]. For example, Asadi *et al.* [21] show that for normal human speech and regardless of the spoken language, the rate of particle emission is affected by loudness of vocalization, ranging from about 1 to 50 particles per second (0.06 to 3 particles per  $\text{cm}^3$ ) for low to high amplitudes. They further indicate that a small fraction of the population acts as “speech superemitters,” consistently releasing an order of magnitude more particles than their peers. Furthermore, Asadi *et al.* [23] indicate that surgical masks and KN95 respirators have been shown to decrease the outward particle emission rates by 90% and 74% on average during speaking and coughing, respectively. However, the efficacy of cloth masks in reducing particle emission rates may be substantially reduced by the need to speak more loudly when wearing such masks. Moreover, Bazant *et al.* [34] have suggested monitoring indoor concentrations of carbon dioxide to quantify the risk of airborne transmission. They proposed a mathematical model to enable predictions of airborne transmission risks from real-time carbon dioxide measurements.

Infectiousness of an epidemic is measured in terms of the reproduction number, which is the number of positive transmissions per infected individual [36–39]. Bazant and Bush [8], in their comprehensive investigation, introduced the indoor airborne reproduction number as the expected number of transmissions in a room of total occupancy  $N$  from a single infected person. According to their definition, the indoor reproduction number is a function of time, and it represents the number of transmissions from the moment the infected person enters the room. With this definition, they were able to convincingly explain explosive spreading of the infection in the super-spreading events and develop guidelines to limit indoor spreading.

By setting the indoor reproduction number to be smaller than a risk threshold, Bazant and Bush [8] obtained an expression for the cumulative exposure time (CET), which they use as a framework to develop social distancing guidelines. CET is the maximum safe duration a group of  $N$  potential receivers can gather in an indoor space with one infected individual, and maintain the reproduction number less than the risk threshold. The fundamental quantity that connects the infected and the receiving persons is the pathogen concentration  $C(r, t)$ , which is the number of virions in nuclei of size  $r - dr/2$  to  $r + dr/2$  in a unit volume of air at the receiver. In addition to pathogen concentration, CET also depends on the volumetric breathing rate of the receiver, the filtration efficiency of the receiver’s mask, and virological factors such as relative transmissibility, and infectivity (see Ref. [8]).

Following the pioneering works of Wells [40] and Riley [41], the assumption of a well-mixed air volume has been used by many others in analyzing the spread of several infectious diseases in indoor spaces [8,42–48]. According to the well-mixed assumption, the ejected nuclei, and the virions contained within, rapidly spread over the entire volume and are available to any receiver at equal probability. This assumption is necessary to pose the problem of viral transmission in a general way to develop safety guidelines for broad applicability. Without the well-mixed assumption, quantities such as pathogen concentration and CET will depend on the specific location of both the infected and the receiving person within the indoor space, thereby substantially complicating further deduction of safety guidelines.

The well-mixed assumption is rooted in the important fact that the flow within indoor spaces is turbulent, due to either natural or forced ventilation, and that turbulence promotes good mixing of the airborne nuclei. Though it is now well understood that turbulence can also de-mix and create preferential regions of much higher concentration than the average value [49], this mechanism is expected to be inactive in the case of airborne nuclei, due to their small Stokes number [50]. It can be expected that a perfect well-mixed state will not be achieved in an indoor space at any reasonable level of ventilation. The limitations of the well-mixed assumption are well recognized by previous modelers. For example, Bazant and Bush [8] point out that the pathogen concentration around a receiver who is located in the direct flow path of an infected person's exhalation can be substantially larger than the average pathogen concentration obtained from the well-mixed assumption. Accordingly, CET for such a receiver will be much smaller than what the guideline, developed based on well-mixed concentration, would recommend. However, there are receiver locations where the pathogen concentration may be much smaller than the well-mixed concentration, and in such cases, the average guideline can be overly restrictive. It should be noted that the well-mixed assumption has also been investigated in the context of cooling and heating of indoor spaces [51,52].

The well-mixed assumption can be separated into the following three related assertions. First, the location of the infected person (*source*) within the indoor volume does not matter. Second, the location of the receiving person (*sink*) does not matter in terms of CET. Third, it follows that the relative position of the infected and the receiving persons (whether it is 6 feet or 60 feet) does not matter as well [8]. This work will evaluate the well-mixed assumption at different levels by (i) comparing the well-mixed model against room-averaged statistics from LES, (ii) monitoring the change in the room-averaged pathogen concentration as the source location is varied within the room, (iii) analyzing the departure of pathogen concentration at different receiver (*sink*) locations from the well-mixed concentration, and (iv) assessing the dependence of pathogen concentration on the distance between the source and sink within the room.

The attractiveness of the well-mixed approach [8,40,41] is its simplicity, while comprehensively incorporating all the relevant flow physics, mask effectiveness, and epidemiological factors. Thus, the well-mixed approach will remain in common use and guide policy decisions regarding social distancing. The present four-level evaluation of the well-mixed assumption will highlight its robustness. Furthermore, it will also point out systematic statistical departures in pathogen concentration from the well-mixed concentration that warrant further attention. These departures can be accurately accounted for with an easily implementable correction factor to quantities such as CET. The well-mixed model will remain the baseline of the present work, and the correction factor may be used to account for additional important aspects such as source to sink separation.

## II. MATHEMATICAL AND NUMERICAL FORMULATION

### A. Fluid phase

We examine the implications of the well-mixed approximation in a canonical room of size  $10\text{ m} \times 10\text{ m} \times 3.2\text{ m}$  with a typical four-way inlet surrounding a central outlet ventilation system that is located on the ceiling at the center of the room [see Fig. 2(E)]. The ventilation system is comprised of four inlets of size  $0.055\text{ m} \times 0.44\text{ m}$  surrounding an outlet of size  $0.6\text{ m} \times 0.6\text{ m}$  [see Fig. 2(E)—inlets in magenta, outlet in green] placed at the center of the ceiling of a  $10\text{ m} \times 10\text{ m} \times 3.2\text{ m}$  room. Three simulations are considered for which air, of density  $\rho_f = 1.2041\text{ Kg/m}^3$  and viscosity  $\mu_f = 1.81 \times 10^{-5}\text{ Ns/m}^2$ , is ejected at a speed of 3.57, 7.14, or 14.28 m/s. These air speeds result in ACH values of 2.5, 5, and 10, respectively, for which the corresponding total inlet Reynolds number  $\text{Re}_{\text{in}} = 4\rho_f U_{\text{in}} A_{\text{in}} / \mu_f$  becomes  $2.30 \times 10^4$ ,  $4.6 \times 10^4$ , and  $9.2 \times 10^4$ . ACH, which has dimensions of  $\text{h}^{-1}$ , stands for air changes per hour and corresponds to the ratio of volumetric flow rate in  $\text{m}^3\text{h}^{-1}$  to the room volume in  $\text{m}^3$ . The average dissipation rate within the room can be estimated from the kinetic energy of the inlet, and the associated Kolmogorov length scale is  $O(150)\mu\text{m}$  for an ACH of 10. The Kolmogorov scale decreases with increasing ventilation

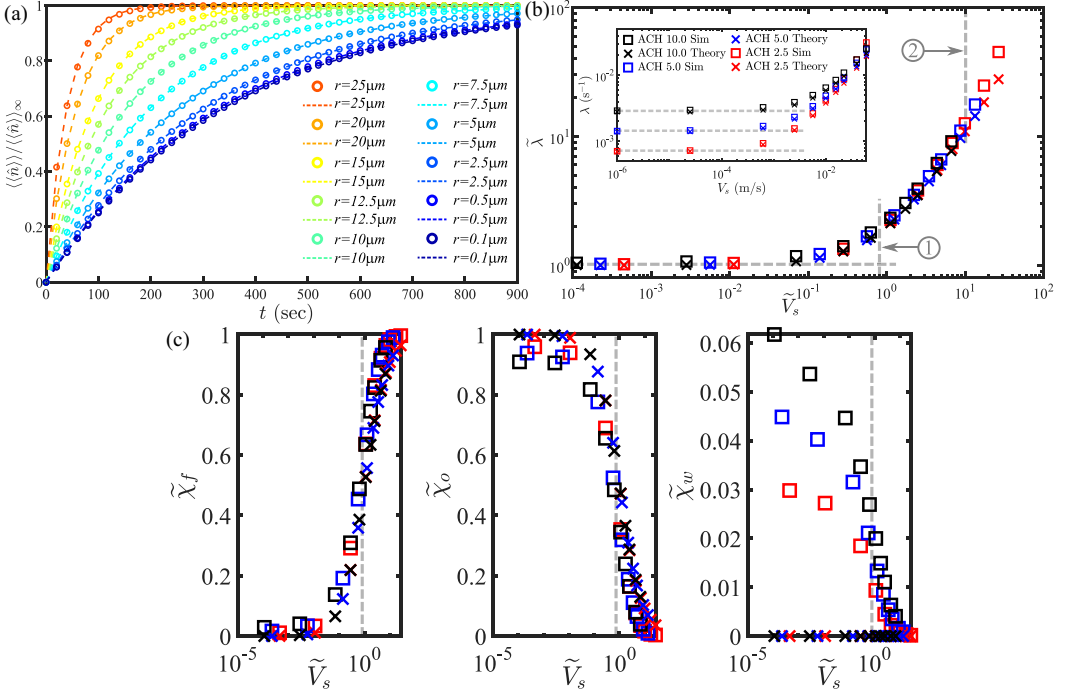


FIG. 1. (A) Decay of nuclei concentration vs time. Simulation data “o” vs exponential fit “—” for ACH = 10. (B) ACH-scaled decay rate  $\tilde{\lambda}$  vs ACH-scaled settling velocity  $\tilde{V}_s$ . The horizontal dashed line represents  $\tilde{\lambda} = 1$ , which corresponds to the theoretical estimate for very small nuclei. Inset: Dimensional  $\lambda$  vs  $V_s$ . The three horizontal lines represent the theoretical estimates for very small nuclei for each ACH value. (C) Proportion of nuclei that exit through the floor ( $\tilde{\chi}_f$ ), the outlet ( $\tilde{\chi}_o$ ), and the walls ( $\tilde{\chi}_w$ ) relative to the total number of nuclei that were removed. The vertical dashed line represents the cutoff size for airborne nuclei in the well-mixed theory.

as  $\text{ACH}^{-3/4}$ . The resolution of the entire range of turbulent length (and time) scales poses a great challenge, even without accounting for the smaller-sized nuclei. Therefore, in the present work we use large eddy simulations (LES, [53]) for the fluid in the room with the nuclei taken into account through the point-particle model (Euler-Lagrange simulations [33,50]).

The gas-phase governing equations are the incompressible Navier–Stokes equations. The filtered gas-phase governing equations have been rigorously derived in the context of Euler-Lagrange multiphase flow simulations [54]. In the present limit of very low droplet volume fraction, the governing equations can be further simplified to obtain the following equations:

$$\nabla \cdot \tilde{\mathbf{u}} = 0, \quad (1)$$

$$\frac{\partial \tilde{\mathbf{u}}}{\partial t} + \tilde{\mathbf{u}} \cdot \nabla \tilde{\mathbf{u}} = -\nabla \tilde{p} + (\nu + \nu_t) \nabla^2 \tilde{\mathbf{u}}, \quad (2)$$

where tilde indicates a filtered variable when used for Eulerian fields. The filtering process introduces an unknown subgrid Reynolds stress term into the filtered momentum equation, which has been closed with the eddy viscosity model, where the turbulent eddy viscosity  $\nu_t$  is obtained using the dynamic Smagorinsky model [55,56]. The above equations are appropriate for the case of an externally forced flow within a room driven by an air conditioning unit. In real situations, there may be additional convective flow within the room induced by local heating due to human presence. Such buoyancy-driven flow is not accounted for in the above governing equations. Although the

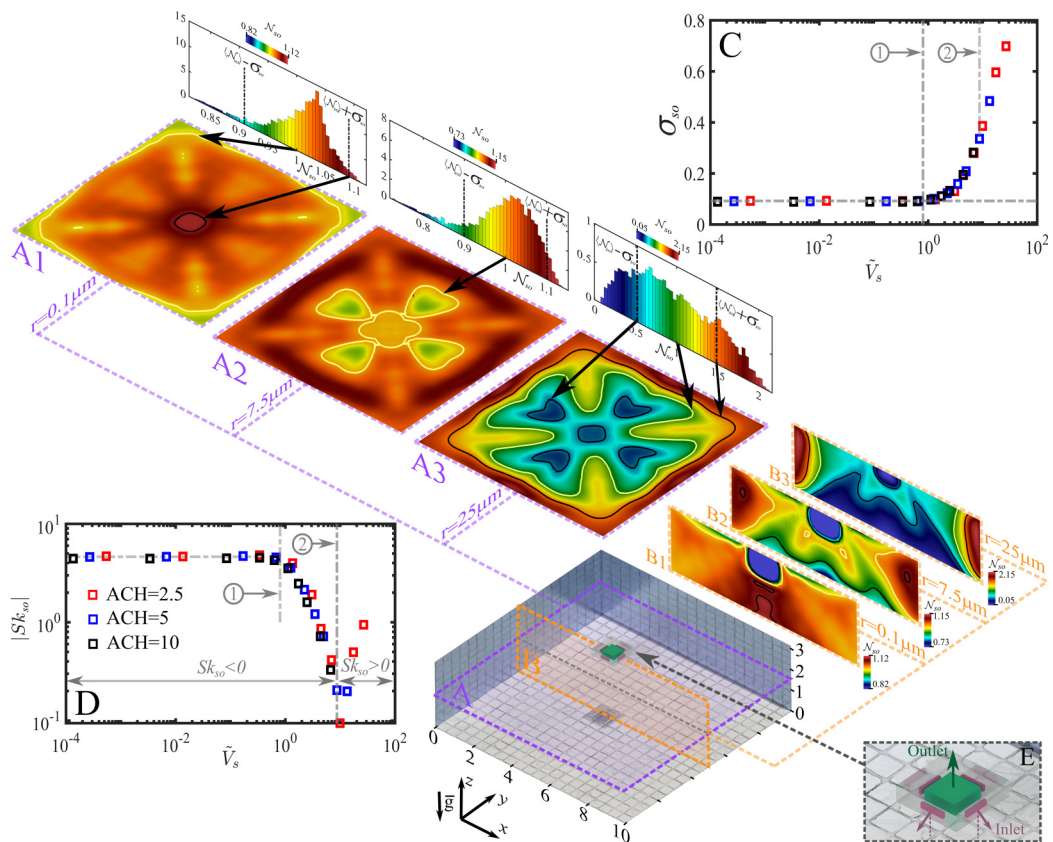


FIG. 2. Concentration from the source perspective. For the ACH = 5 case, composite plot of contours of  $\mathcal{N}_{s0}$  at (A)  $z = 1.6$  m (violet planes) and (B)  $y = 5$  m (orange planes), for different nuclei sizes (A1–A3 and B1–B3). Also, for planes A1–A3, we show the probability density function (PDF) for the scaled concentration  $\mathcal{N}_{s0}$  for each nuclei size in the entire room. Note that the PDFs and contour plots are colored by values of  $\mathcal{N}_{s0}$ . Furthermore, the insets show the (C) standard deviation  $\sigma_{s0}$  and (D) absolute value of skewness  $|Sk_{s0}|$  of the PDFs as a function of scaled settling  $\tilde{V}_s$ , for all cases.

inclusion of the buoyancy efforts in the simulations is straightforward, here we have chosen to ignore the buoyancy-induced flow, since its inclusion requires specification of additional details, such as the location of the heat source and the rate of heat emission. As we will see later, such problem specific details prevent us from seeking a broad generalization to the well-mixed theory. Furthermore, based on the present results, the average droplet nuclei within the room, at the level of the well-mixed theory, depends only on the settling rate and the rate at which air flow exits the room. Extra circulation within the room due to buoyancy will only play a secondary role. Of course this point needs to be verified.

### B. Droplet nuclei phase

Each ejected nuclei is individually tracked. In the present context of dilute two-phase flow, direct (collision) and indirect (fluid-mediated) interactions within the dispersed phase are neglected. The governing equations for the position and velocity of the  $l$ th nucleus are given by

$$\frac{d}{dt} \begin{bmatrix} \mathbf{X}_l \\ \mathbf{V}_l \end{bmatrix} = \begin{bmatrix} \mathbf{V}_l \\ \mathbf{F}_l/m_l \end{bmatrix}. \quad (3)$$

Here,  $m_l = 4\pi r_l^3 \rho_p / 3$  is the mass of the  $l$ th nucleus, where  $\rho_p = 1000 \text{ Kg/m}^3$  is the density of the nucleus of radius  $r_l$ .

Due to the relatively large density ratio ( $\rho = \rho_p / \rho_f$ ), forces apart from the quasisteady and gravitational forces are neglected. As a result, the total force  $\mathbf{F}_l$  acting on the  $l$ th nucleus becomes the summation of the quasisteady ( $\mathbf{F}_{\text{qs},l}$ ), and gravity-buoyancy ( $\mathbf{F}_{\text{g},l}$ ) forces, i.e.,

$$\mathbf{F}_l = \mathbf{F}_{\text{qs},l} + \mathbf{F}_{\text{g},l} = 6\pi\mu_f r_l (\mathbf{u}(\mathbf{X}_l) - \mathbf{V}_l) \Phi(\text{Re}_l) + V_l (\rho_p - \rho_f) |\mathbf{g}|, \quad (4)$$

where  $V_l = 4\pi r_l^3 / 3$  is the volume of the  $l$ th nucleus. The Reynolds number of the  $l$ th nucleus is computed as  $\text{Re}_l = 2\rho_f |\mathbf{u}(\mathbf{X}_l) - \mathbf{V}_l| r_l / \mu_f$ . The function  $\Phi(\text{Re}_l) = 1 + 0.15 \text{Re}_l^{0.687}$  is the finite Reynolds number drag correction, which depends on the nucleus Reynolds number. In Eq. (4), the fluid velocity  $\mathbf{u}$  is evaluated at the center of the  $l$ th nucleus ( $\mathbf{X}_l$ ) through interpolation. Since we have filtered the effect of eddies smaller than the grid size, this fluid velocity evaluated at the nucleus center requires an additional contribution. It is computed as  $\mathbf{u}(\mathbf{X}_l) = \tilde{\mathbf{u}}(\mathbf{X}_l) + \mathbf{u}'(\mathbf{X}_l)$ , where the resolved part  $\tilde{\mathbf{u}}$  reflects the macroscale flow computed in the Euler-Lagrange LES, and  $\mathbf{u}'$  is the contribution from the unresolved subgrid eddies. With this in mind, we compute the perturbation velocity using the Langevin model [57–61]

$$\mathbf{u}'[\mathbf{X}_l(t + \Delta t), t + \Delta t] = \left[ 1 - \left( \frac{1}{2} + \frac{3C_0}{4} \right) \frac{C_s^2 |\tilde{\mathcal{S}}|}{2C_Y} \Delta t \right] \mathbf{u}'[\mathbf{X}_l(t), t] + \sqrt{C_0/3} \tilde{\varepsilon} \Delta t f_w \xi, \quad (5)$$

where  $\tilde{\varepsilon} = \nu_t |\tilde{\mathcal{S}}|^2$  is the dissipation rate that depends on the filtered strain rate tensor  $\tilde{\mathcal{S}}$ , and  $\Delta t$  is the simulation time step. The wall filter function  $f_w$  is unity over most of the computational domain except within 100 wall units close to any boundary, where it goes to zero in an anisotropic manner [61]. Parameters  $C_s = 0.18$ ,  $C_0 = 2.1$ , and  $C_Y = 0.039$  are obtained from previous works [62,63] and  $\xi \sim \mathcal{N}(0, 1)$  is a Gaussian-distributed random variable.

For nuclei smaller than  $10 \mu\text{m}$ , as inertial effects are negligible, an equilibrium-Lagrangian model [64] is used, where the nuclei trajectories are obtained from

$$d\mathbf{X}_l/dt = \mathbf{u}(\mathbf{X}_l) + \mathbf{V}_{s,l}. \quad (6)$$

The velocity of the  $l$ th nucleus becomes the superposition of the fluid velocity at the nucleus center and the nucleus settling velocity. The latter is computed as

$$\mathbf{V}_{s,l} = \frac{r_l^2 (\rho + 0.5)}{18\mu_f \Phi(\text{Re}_{p,l})} \left( 1 - \frac{3}{2\rho + 1} \right) \mathbf{g}, \quad (7)$$

where  $\text{Re}_{p,l} = 2\rho_f |\mathbf{V}_{s,l}| r_l / \mu_f$ .

It should be noted that the ejected droplets, irrespective of the mode of ejection (speaking, singing, etc.), rapidly evaporate to their final fully evaporated droplet nuclei state within a second or so after ejection [6,65]. As a result, the present room-scale simulations consider only the dispersion of the fully evaporated airborne droplet nuclei within the indoor space. A large number of droplet nuclei of 10 different sizes is introduced into the room. Their position and velocity are advanced in time according to Eq. (3). By considering only the post-evaporation state, the size of each droplet nuclei remains the same over time. In doing so, we keep our approach general without restricting it to specific ambient conditions. The present results remain general and can be applied to any specific ejection scenario and ambient condition by appropriately choosing the initial size spectra of the droplet nuclei ejected by the “source” to correctly reflect the physiological nature of the ejection process and the ambient conditions under consideration. In the present work, we also assume the viral load to be proportional to the volume of the droplet nuclei [30].

### C. Numerical methodology and simulation details

The gas-phase LES equations are solved using a highly scalable spectral element solver [66]. The Lagrangian droplets are solved using the highly scalable point-particle library ppicIF [67].

The domain is discretized using  $60 \times 60 \times 16$  hexahedral elements (of polynomial order five) with  $6^3$  Gauss-Lobatto-Legendre (GLL) grid points within each element. This results in a total of 12.4 million grid points, with an average of 19 grid points below 30 wall-units, near the four side walls. A Dirichlet boundary condition velocity is imposed at the inlets [see Fig. 2(E)], while an open boundary condition is used at the outlet [68]. No-slip and no penetration conditions are used at the lateral walls, floor, and ceiling. The turbulent flow is allowed to reach a statistically steady-state before introducing the nuclei to the simulation. 20 million nuclei of ten different radii, ranging from 100 nm to 25  $\mu\text{m}$ , are randomly but uniformly positioned within the room. The nuclei are then transported by the flow, where they would eventually settle to the floor, deposit on the walls and ceiling, or be removed by the outlet. We performed three simulations with different ACH values of 2.5, 5, and 10. The cost of each simulation amounts to approximately 221,000 CPU hours.

### III. STATISTICAL FRAMEWORK

Consider the scenario of an infected person (source) entering the room at  $t = 0$  and located at  $\mathbf{x}_{\text{so}}$  inside the room. The risk of infection for a stationary receiving person (sink) located at  $\mathbf{x}_{\text{si}}$  depends on the local pathogen concentration  $c(t, \mathbf{x}_{\text{si}}, \mathbf{x}_{\text{so}})$ , measured as number of virions per volume. Following Ref. [8]  $c(t, \mathbf{x}_{\text{si}}, \mathbf{x}_{\text{so}}) = \int n(t, \mathbf{x}_{\text{si}}, \mathbf{x}_{\text{so}}, r)V(r)c_v(r)dr$ , where the integration is over all possible radii of the nuclei,  $V(r) = 4\pi r^3/3$  is the volume of a droplet nucleus of radius  $r$ , and  $c_v(r)$  is the size-dependent concentration of virion inside the nuclei [4,69,70]. Here  $n(t, \mathbf{x}_{\text{si}}, \mathbf{x}_{\text{so}}, r)$  is the concentration of nuclei of radius  $r$ , measured as the number of nuclei per volume of air per size, at the sink location as a function of time, conditioned on the source being located at  $\mathbf{x}_{\text{so}}$ . The nuclei concentration can further be expressed as  $n(t, \mathbf{x}_{\text{si}}, \mathbf{x}_{\text{so}}, r) = \hat{n}(t, \mathbf{x}_{\text{si}}, \mathbf{x}_{\text{so}}, r)Q_b n_{\text{so}}(r)$ , where  $Q_b$  is the breathing rate of the infected person and  $n_{\text{so}}(r)$  is the concentration of exhaled nuclei of radius  $r$  that remain airborne. With this definition, the fundamental quantity to be analyzed in this study is  $\hat{n}(t, \mathbf{x}_{\text{si}}, \mathbf{x}_{\text{so}}, r)$ , which corresponds to the normalized nuclei concentration at the sink location  $\mathbf{x}_{\text{si}}$  as a function of time for a steady injection rate of 1 nucleus of radius  $r$  per second by a source at  $\mathbf{x}_{\text{so}}$ . Due to the inhomogeneous nature of the indoor flow,  $\hat{n}$  depends on the specific locations of both the source and the sink.

We denote the corresponding quantity in the well-mixed theory as  $\hat{n}_{\text{wm}}(t, r)$ , which corresponds to the well-mixed concentration of nuclei of radius  $r$  at time  $t$ . This concentration is the same at all sink locations within the room and is also independent of the source location. However, complete characterization of  $\hat{n}$  depends on all possible combinations of source and sink locations within the room. Furthermore, due to the turbulent nature of the flow, for a given source and sink combination,  $\hat{n}$  will exhibit random fluctuations as a function of time. These random fluctuations are nonexistent for  $\hat{n}_{\text{wm}}$  due to the double averaging over all possible source and sink locations. In essence,  $\hat{n}$  is a far more complex quantity that is both a random function of time and dependent on seven additional degrees of freedom ( $r, \mathbf{x}_{\text{so}}$  and  $\mathbf{x}_{\text{si}}$ ).

The well-mixed theory can now be evaluated at four different levels. (i) In the simulations, the well-mixed concentration can be approximated with a double average over all possible source and sink locations as

$$\langle\langle \hat{n} \rangle\rangle(t, r) = \int_{\mathbf{x}_{\text{so}}} \int_{\mathbf{x}_{\text{si}}} \hat{n}(t, \mathbf{x}_{\text{si}}, \mathbf{x}_{\text{so}}, r) d\mathbf{x}_{\text{si}} d\mathbf{x}_{\text{so}} / \mathcal{V}^2, \quad (8)$$

where the integrals are over the entire room of volume  $\mathcal{V}$ . A comparison of  $\hat{n}_{\text{wm}}$  with  $\langle\langle \hat{n} \rangle\rangle$  will reveal the strength of the simple model used in past studies [8] in making predictions at the room-averaged level. (ii) The simulation results when averaged only over all possible sink locations as

$$\langle \hat{n} \rangle_{\text{si}}(t, \mathbf{x}_{\text{so}}, r) = \int_{\mathbf{x}_{\text{si}}} \hat{n}(t, \mathbf{x}_{\text{si}}, \mathbf{x}_{\text{so}}, r) d\mathbf{x}_{\text{si}} / \mathcal{V} \quad (9)$$



will reveal the dependence of room-averaged pathogen concentration on the location of the source. (iii) The simulation results when averaged only over all possible source locations as

$$\langle \hat{n} \rangle_{\text{so}}(t, \mathbf{x}_{\text{si}}, r) = \int_{\mathbf{x}_{\text{so}}} \hat{n}(t, \mathbf{x}_{\text{si}}, \mathbf{x}_{\text{so}}, r) d\mathbf{x}_{\text{so}} / \mathcal{V} \quad (10)$$

will reveal the dependence of pathogen concentration on the location of the sink. (iv) At the final level, the simulation results  $\hat{n}(t, \mathbf{x}_{\text{si}}, \mathbf{x}_{\text{so}}, r)$  without any averaging over source or sink location will be compared against  $\langle \langle \hat{n} \rangle \rangle(t, r)$  to reveal if there are source-sink combinations that are 1, 2, 4, or 8 m apart that are substantially more prone to disease spreading than what is predicted based on the well-mixed assumption.

To make reliable inferences from the above comparisons, it is imperative that the different quantities being compared be evaluated with adequate statistical convergence. Statistical convergence is easier to obtain in the double-averaged  $\langle \langle \hat{n} \rangle \rangle$  and in the single-averaged  $\langle \hat{n} \rangle_{\text{si}}$  or  $\langle \hat{n} \rangle_{\text{so}}$ . Statistical convergence is harder in case of unaveraged  $\hat{n}$ .

We must point out that each source and sink location within the room presents a unique situation for airborne viral dispersion. Therefore, to fully evaluate the statistical behavior of  $\hat{n}(t, \mathbf{x}_{\text{si}}, \mathbf{x}_{\text{so}}, r)$ , all possible values of  $\mathbf{x}_{\text{si}}$  and  $\mathbf{x}_{\text{so}}$  must be considered. A naive approach will be to perform a large number of LES, with each simulation focusing on one particular source-sink combination. However, given the computational cost of an individual LES, such an approach of performing a large number of LES would be prohibitively expensive. Clearly, an LES of the droplet nuclei dispersion process from an individual to another individual in the room is computationally well within reach, since such simulations are quite similar to those reported in the present manuscript.

We surmount these challenges with a novel *statistical overloading technique*. We perform a single large eddy simulation with an abundance of nuclei of varying size, far in excess of what is typically ejected by an infected individual. The one-way coupled nature of the problem (i.e., the suspended nuclei do not alter the flow) allows for this overloading. By distributing and monitoring the nuclei over the entire volume of the indoor space, we obtain the requisite converged statistical information for any source-sink combination.

We should also note that we are tracking all of the 20 million droplet nuclei in each simulation. Whether they deposit on the ground, the sidewalls, or the ceiling, or whether they exit through the outlet, they are all tracked from the point of ejection to the point of exit. We could obtain some of the statistics presented in this work using a passive scalar field (with added settling velocity) with an Euler-Euler (EE) framework [64]. However, with the EE framework we would not be able to precisely track dispersion of droplets from a source to a sink. Lagrangian markers allow us to track individual nuclei of various sizes from any source location to any sink location. This would not be possible with a scalar field and would thus defeat the purpose of the present work.

While the statistics are computed based on a large ensemble of droplet nuclei, in the evaluation of the infectiveness of an individual entering a room, we use exactly the same number density of droplet nuclei for each expelled event as in Ref. [8]. The ejected droplet spectra for different ejection activities were obtained from the experimental work of Ref. [71].

By understanding how pathogen concentration varies within the indoor space under different source and sink scenarios, it is possible to extend the well-mixed theory to develop enhanced guidelines that can be adapted to specific scenarios. This additional information on pathogen concentration variation within an indoor space is what we plan to systematically develop with the above defined four levels of comparison. By choosing the normalized nuclei concentration as the basis of comparison with the well-mixed theory of Ref. [8], we fully leverage their comprehensive prediction framework. Quantities such as CET, which are important for the development of safety guidelines, can be readily evaluated taking into account how local pathogen concentration departs from the well-mixed value with a simple correction factor. This simple scaling based on local pathogen concentration is possible because all other factors such as breathing rate, mask efficiency, and epidemiological parameters can be taken to remain the same.

## IV. SOURCE AND SINK-AVERAGED STATISTICS

According to the well-mixed theory, the room-averaged nuclei concentration steadily increases upon the arrival of the infected person and reaches a steady-state when the rate of nuclei exhalation balances the rate at which the nuclei exit the room through the outlet and by settling to the floor. The time evolution of normalized nuclei concentration is expressed as [8,15,40,41]

$$\hat{n}_{\text{wm}}(t, r) = \frac{1}{\lambda_{\text{wm}}(r)\mathcal{V}} \{1 - \exp[-\lambda_{\text{wm}}(r)t]\}, \quad (11)$$

where the decay rate is given by

$$\lambda_{\text{wm}}(r) = \frac{\text{ACH}_{\text{ef}}(r)}{3600} + \frac{V_s(r)}{H}, \quad (12)$$

where  $V_s(r)$  and  $H$  represent the size-dependent droplet settling velocity and room height, respectively. The effective ACH can be expressed as  $\text{ACH}_{\text{ef}}(r) = \text{ACH}_{\text{nr}} + \text{ACH}_r \eta_f(r)$ , where ventilation is divided into a recycled part ( $\text{ACH}_r$ ) and a nonrecycled part ( $\text{ACH}_{\text{nr}}$ ), and  $\eta_f(r)$  is the size-dependent efficiency of filtration of the recycled air. The rate of viral removal by deactivation has been taken to be zero in the present simulations. The theory thus splits the decay rate into two contributions, the first due to ventilation, and the second due to settling. The settling velocity can be expressed as  $V_s(r) = 2\rho r^2 g / (9\nu_f \Phi)$  [19], where  $\rho \approx 10^3$  is the ratio of ejected fluid density to air density,  $g$  the gravitational acceleration,  $\nu_f$  the kinematic viscosity of air, and  $\Phi$  the finite Reynolds number drag correction, which deviates from unity for droplets of radius greater than  $5 \mu\text{m}$ . For small droplets of settling velocity  $V_s \ll H$  ( $\text{ACH}_{\text{ef}}/3600$ ) the decay rate is mainly due to ventilation, whereas for large droplets of  $V_s \gg H$  ( $\text{ACH}_{\text{ef}}/3600$ ) the decay rate is mainly through floor deposition.

The normalized nuclei concentration obtained from the  $\text{ACH} = 10$  simulation, double-averaged over all source and sink locations, is shown in Fig. 1(A). Note the concentration has been divided by the terminal value of  $\langle\langle\hat{n}\rangle\rangle_{\infty}(r) = \langle\langle\hat{n}\rangle\rangle(t \rightarrow \infty, r) = 1/[\lambda(r)\mathcal{V}]$  and thus the plots of all ten sizes approach unity with increasing time. The excellent agreement with the exponential fits demonstrates that Eq. (11) can adequately describe the LES results as well.

The decay rate  $\lambda$ , obtained from each exponential fit, is plotted as a function of settling velocity for the ten different nuclei sizes and three different ACH values in the inset of Fig. 1(B). An excellent collapse across the different ACH cases is obtained by plotting the nondimensional decay rate as a function of nondimensional settling velocity in Fig. 1(B), where

$$\tilde{\lambda} = \frac{3600}{\text{ACH}} \lambda \quad \text{and} \quad \tilde{V}_s = \frac{3600 V_s}{\text{ACH} H}. \quad (13)$$

Also plotted in the figure is  $\tilde{\lambda}_{\text{wm}}$  given in Eq. (12). It is remarkable that the simple theory of Bazant and Bush [8] is able to capture the decay rate quite accurately over a wide range of nuclei sizes (and settling velocities). It can be seen that in the limit of very small nuclei the theoretical decay rate is within 1% of the simulation data. It should be borne in mind that the simulation results are somewhat dependent on the room size, shape and ventilation inlet and outlet locations.

By equating the characteristic times for droplet settling and removal through ventilation, Bazant and Bush [8] defined a critical droplet radius  $r_c = \sqrt{9\nu_f(\text{ACH})H\Phi/(7200\rho g)}$ , whose critical nondimensional settling velocity is  $\tilde{V}_{\text{sc}} = 1$  (marked by a dashed vertical line). Droplet nuclei of size  $r > r_c$  were assumed to settle too fast and were not included in their evaluation of pathogen concentration. It is quite impressive that the theory is able to accurately predict the simulated decay rate even for larger nuclei of  $\tilde{V}_s \approx 10\tilde{V}_{\text{sc}}$ . For larger droplets, we observe the simulated nuclei decay rate to increase above the theoretical prediction.

The fact that larger droplets may remain airborne can be of significance. Such droplets exit the room mostly by gravitational settling, so that their  $\lambda(r) \approx V_s(r)/H$ , which means their  $\langle\langle\hat{n}\rangle\rangle_{\infty}(r) \approx H/[V_s(r)\mathcal{V}]$ . If we combine this estimate of nuclei concentration with that for settling velocity

$V_s(r) \propto r^2$  and droplet volume  $V(r) \propto r^3$ , then we obtain the normalized volumetric concentration to scale as  $\langle \langle \hat{n} \rangle \rangle_\infty(r) V(r) \propto r$ . This normalized concentration must be multiplied by  $Q_b n_{s0}(r)$  to obtain the unnormalized volumetric concentration of airborne nuclei. Therefore, the importance of larger droplets depends on whether  $n_{s0}(r)$  decays faster than  $1/r$  in the size range corresponding to  $\tilde{V}_s > 1$ . We shall discuss this further when we consider implications to guidelines.

In addition to capturing the total decay rate with remarkable accuracy, the theory is also able to predict how droplet nuclei exit the room as shown in Fig. 1(C). In the present LES, we observe that a more representative model for the decay rate is

$$\lambda(r) = \lambda_o(r) + \lambda_f(r) + \lambda_w(r), \quad (14)$$

which includes three exit mechanisms: through ventilation outlet, by gravitational (floor) settling, and by wall deposition. With the present Langevin model that accounts for the effects of subgrid turbulence, we observe  $\tilde{\chi}_w(r) = \lambda_w(r)/\lambda(r)$  to constitute up to 3% to 6% of the total amount of nuclei that exit the room. We also observe that the amount of wall deposition, albeit small, increases with ACH.

The ratios  $\tilde{\chi}_f$ ,  $\tilde{\chi}_o$ , and  $\tilde{\chi}_w$  are plotted in Fig. 1(C), along with the well-mixed theoretical estimates given in Eq. (12). Note that the three ratios add up to unity,  $\tilde{\chi}_f + \tilde{\chi}_o + \tilde{\chi}_w = 1$  and that  $\tilde{\chi}_{w, \text{wm}} = 0$  in the well-mixed theory. When plotted in nondimensional quantities, the results for the three different ACH show excellent collapse and become solely a function of  $\tilde{V}_s$  for  $\tilde{V}_s \gtrsim 0.1$ . The effect of ACH is however apparent for  $\tilde{V}_s \lesssim 0.1$ , where wall deposition increases with ACH, albeit by a few percent. The increased wall deposition is counter-balanced by a decrease in ventilation outlet removal. For  $\tilde{V}_s \lesssim 0.1$  the airborne nuclei can be considered small, and for a fixed ACH, the ratios take nearly constant values.

The largest disparity between the simulation results (shown as squares) and the theoretical estimates (shown as crosses) is observed for  $\tilde{\chi}_w$ . This difference is the result of the fact that the well-mixed theory does not account for wall deposition. The theory also overpredicts  $\tilde{\chi}_o$  by about 5% to 15% and underpredicts the floor settling by nearly the same amount.

It is important to note that when nuclei removal by wall deposition is taken together with exit through ventilation outlet, the well-mixed theory is quite accurate and incurs only a small error. The ability to separate nuclei removal through wall and floor deposition versus ventilation can become important when accounting for air recycling and filtration efficiency.

## V. SINK-AVERAGED STATISTICS: SOURCE PERSPECTIVE

In this section we place the source, which is releasing virus-laden nuclei at a constant rate, at a specific location within the room and investigate the effect of source location on the room-averaged normalized nuclei concentration (i.e., we average over all possible sink locations). To simplify the investigation and remove  $t$  as a parameter, we only focus on the steady-state concentration long after the source has entered the room (i.e., as  $t \rightarrow \infty$ ). We plan to obtain the sink-averaged statistics  $\langle \hat{n} \rangle_{\text{si}, \infty}(\mathbf{x}_{s0}, r)$  for the different nuclei sizes as a function of source location and compare the results with the double-averaged quantity  $\langle \langle \hat{n} \rangle \rangle_\infty(r) = 1/[\lambda(r)\mathcal{V}]$ .

The ratio  $\mathcal{N}_{s0}(\mathbf{x}_{s0}, r) = \langle \hat{n} \rangle_{\text{si}, \infty}(\mathbf{x}_{s0}, r) / \langle \langle \hat{n} \rangle \rangle_\infty(r)$  is presented in Fig. 2 as a composite plot for the ACH = 5 case. Contours of the 3D field  $\mathcal{N}_{s0}(\mathbf{x}_{s0}, r)$  are shown at (A)  $z = 1.6$  m (violet planes) and (B)  $y = 5$  m (orange planes), for different nuclei sizes (A1–A3 and B1–B3). We also show the probability density function (PDF) of  $\mathcal{N}_{s0}$  for each nuclei size sampled over all source locations within the room. Note that the PDFs are colored by values of  $\mathcal{N}_{s0}$ , and that the mean value of  $\mathcal{N}_{s0}$ , averaged over all the source locations, is 1 by definition. Therefore, regions where  $\mathcal{N}_{s0} < 1$  indicate source locations that are relatively well ventilated where the resulting sink-averaged concentration is lower than the room average value. However, regions where  $\mathcal{N}_{s0} > 1$  indicate source locations that are relatively poorly ventilated where the resulting sink-averaged concentration is higher. Thus, it is of interest to examine the spread of  $\mathcal{N}_{s0}$  as given in the PDFs.

Figure 2(C) shows the standard deviation  $\sigma_{so}$  and Fig. 2(D) shows the absolute value of skewness  $|\text{Sk}_{so}|$  of the PDFs as a function of the scaled settling velocity  $\tilde{V}_s$  for all cases. We observe three regimes: **Regime I** ( $\tilde{V}_s \lesssim 1$ ): Bazant and Bush [8] considered only small nuclei, demarcated by the dashed grey lines marked 1 in Figs. 2(C) and 2(D), to remain airborne. These small nuclei exhibit a Gaussian-like distribution with a small constant standard deviation of  $\approx 10\%$  and a left-sided tail [i.e., negative skewness  $\text{Sk}_{so}$ —see Fig. 2(D)]; the small value of  $\sigma_{so}$  supports the assertion that these small nuclei are well-mixed, independent of the source location. As an example of small nuclei, if we focus on  $r = 0.1 \mu\text{m}$  [Fig. 2(A1) and 2(B1)], a characteristic distribution displaying the dihedral symmetry of the square planform is seen in Fig. 2(A1). The contour values at this elevation of  $z = 1.6 \text{ m}$  are quite close to unity supporting the well-mixed assumption. We observe that  $\mathcal{N}_{so}$  is relatively large right at the center of the room (below the outlet), but small near the side walls and room corners.

**Regime II** ( $1 \lesssim \tilde{V}_s \lesssim 10$ ): For these intermediate size nuclei,  $\sigma_{so}$  increases and skewness decreases up until  $\tilde{V}_s \lesssim 10$  (demarcated by the dashed grey lines marked 2), where  $\text{Sk}_{so} \approx 0$ . As can be seen from Figs. 2(A2) and 2(B2), for the  $r = 7.5 \mu\text{m}$  nuclei, deviation from the well-mixed assumption remains small. From the horizontal and vertical contour plots we observe that the largest local concentration has shifted to the middle of the side walls, while the lowest concentrations are in the four inflow jets of the ventilation system and along the room diagonals.

**Regime III** ( $\tilde{V}_s > 10$ ): We consider even larger droplets, since the LES simulations have revealed small, but nonzero, concentrations of such nuclei within the room. Clearly, the well-mixed assumption is not appropriate for these large nuclei, since local concentrations can be substantially larger or smaller than the mean. The pattern is similar to that of intermediate size nuclei, but the amplitude of variation is much higher. The largest concentrations are near the central portions of the four walls, which contributes to a long positive tail of the PDF and a positive skewness. Regions of concentrations that are much lower than the mean are observed in the inflow jet regions and directly below the ventilation system. For nuclei of size  $r = 25 \mu\text{m}$ , it is striking how detrimental it is for the infected person to stand near the wall, right in the path of the inlet jet. Room-averaged concentrations [see Figs. 2(A3) and 2(B3)] with such a source placement are  $2.5\times$  larger than the mean concentration. In contrast, the room-averaged concentration when the source moves farther from the wall can decrease by about an order of magnitude to a value of  $0.3\langle\hat{n}\rangle_\infty$  as indicated by the dark-blue colored regions.

## VI. SOURCE-AVERAGED STATISTICS: SINK PERSPECTIVE

In this section, we consider the receiving person (sink) to be placed at a specific location within the room. The purpose is to evaluate the virus-laden nuclei concentration that the receiving person would be subjected to. The concentration is averaged over all possible placements of the infected person within the room. In the previous section, we raised the following question: *Provided the receiver location is unknown, are there preferred source locations within the room that could minimize or maximize the probability of infection?* We addressed the question by averaging the nuclei concentration over all possible sink locations. In this section, we ask the inverse question: *Provided the source location is unknown, are there preferred receiver locations within the room that could minimize or maximize the probability of infection?* Here too, we address the question by averaging over all possible source locations.

Again, we only focus on the steady-state concentration long after the source has entered the room. We obtain the source-averaged statistics  $\langle\hat{n}\rangle_{so,\infty}(\mathbf{x}_{si}, r)$  for the different sizes as a function of sink location and compare the results with the double-averaged quantity  $\langle\langle\hat{n}\rangle\rangle_\infty(r) = 1/[\lambda(r)\mathcal{V}]$ . The ratio  $\mathcal{N}_{si}(\mathbf{x}_{si}, r) = \langle\hat{n}\rangle_{so,\infty}(\mathbf{x}_{si}, r)/\langle\langle\hat{n}\rangle\rangle_\infty(r)$  is presented in Fig. 3 as a composite plot for the  $\text{ACH} = 2.5$  case. Contours of the 3D field  $\mathcal{N}_{si}(\mathbf{x}_{si}, r)$  are shown as contours at (A)  $z = 1.6 \text{ m}$  (violet planes) and (B)  $y = 5 \text{ m}$  (orange planes), for different nuclei sizes (A1–A3 and B1–B3). We also plot the PDF of  $\mathcal{N}_{si}$  for each nuclei size sampled over all sink locations within the room. The mean value of  $\mathcal{N}_{si}$  is 1 by definition. Therefore, regions where  $\mathcal{N}_{si} < 1$  indicate sink locations that are

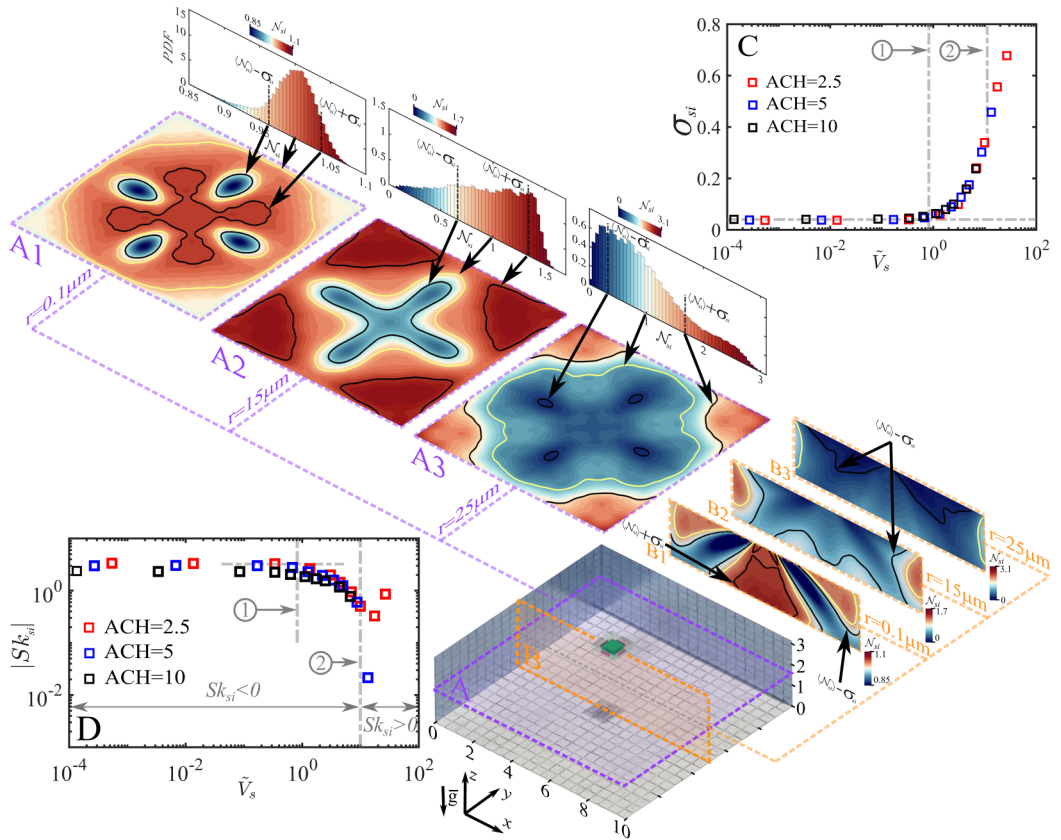


FIG. 3. Concentration from the receiver's perspective. For the ACH = 2.5 case, composite plot of contours of  $\mathcal{N}_{si}$  at (A)  $z = 1.5\text{m}$  (violet planes) and (B)  $y = 5\text{m}$  (orange planes), for different nuclei sizes (A1–A3 and B1–B3). Also, for planes A1 to A3, we show the probability density function (PDF) for the scaled concentration  $\mathcal{N}_{si}$  for each nuclei size in the entire room. Note that the PDFs and contour plots are colored by values of  $\mathcal{N}_{si}$ . Furthermore, the insets show (C) the standard deviation  $\sigma_{si}$  and (D) absolute value of skewness  $|\text{Sk}_{si}|$  of the PDFs as a function of scaled settling  $\tilde{V}_s$ , for all cases.

relatively less prone to infection. However, regions where  $\mathcal{N}_{si} > 1$  indicate sink locations that are relatively more prone to infection.

The inset C shows the standard deviation  $\sigma_{si}$  and the inset D shows the absolute value of skewness  $|\text{Sk}_{si}|$  of the PDFs as a function of scaled settling  $\tilde{V}_s$ . Although there are quantitative differences between Figs. 2 and 3, the qualitative behavior of nuclei concentration variation within the room is quite similar. Again the results show three different regimes. **Regime I** ( $\tilde{V}_s \lesssim 1$ ) exhibits a Gaussian-like distribution with a small constant standard deviation of  $\approx 5\%$  and a left-sided tail (i.e., negative skewness—see inset D); The small value of  $\sigma_{si}$  reinforces the notion that small nuclei are well-mixed independent of the sink location. We observe a characteristic cross-pattern formed by the yellow contour of  $\mathcal{N}_{si}$  in Fig. 2(A1) for the  $r = 0.1\ \mu\text{m}$  nuclei. Contour lines of  $\pm\sigma_{si}$  are also shown. The negative skewness of the distribution supports the observation of a low concentration in a large portion of the room, mainly near the walls and along the inlet jets [see Figs. 2(A1) and 2(B1)].

**Regime II** ( $1 \lesssim \tilde{V}_s \lesssim 10$ ):  $\sigma_{si}$  increases and skewness decreases up until  $\tilde{V}_s \lesssim 10$  (demarcated by the dashed grey lines marked 2), where  $\text{Sk}_{si} \approx 0$ . As can be seen from Figs. 2(A2) and 2(B2), for the  $r = 15\ \mu\text{m}$  nuclei, deviation from the well-mixed assumption is somewhat larger, and the PDF acquires a bimodal distribution. From the horizontal contour plot we can observe that the largest

local concentration has shifted to the corners, while the lowest concentrations are in the four inflow jets of the ventilation system and directly below the ventilation system. Furthermore, the two modes of the PDF appear at slightly higher concentrations than  $\pm\sigma_{\text{si}}$ .

**Regime III** ( $\tilde{V}_s > 10$ ): The well-mixed assumption is not appropriate, since local concentrations can be substantially larger or smaller than the mean. Standard deviation seems to start plateauing and skewness becomes positive [right-sided tail—see Fig. 2(A3)]. The pattern is similar to intermediate size nuclei, but the amplitude of variation is much higher. The largest concentrations are in the room corners, which contribute to a long positive tail of the PDF and a positive skewness. Much lower-than-average concentrations are observed in the inflow jet regions and directly below the ventilation system.

## VII. STATISTICS FOR SPECIFIED SOURCE-SINK SEPARATIONS

In this section we consider specific combinations of source and sink locations and evaluate the probability of normalized nuclei concentration being substantially different from that of the well-mixed theory. This approach will allow us to investigate specific source-to-sink distances, such as 2 or 4 m, which was not possible in the earlier sections that involved double (source and sink) or single (source or sink) averaging. However, the challenge with allowing the source and sink to vary over all possible locations within the room is that it involves six degrees of freedom ( $x$ ,  $y$ , and  $z$  location of the source and sink) apart from nuclei size. To simplify the analysis, we will consider the distance between the source and the sink,  $d = |\mathbf{x}_{\text{si}} - \mathbf{x}_{\text{so}}|$  to be a key parameter and consider all source-sink combinations that are separated by a distance  $d$ . [72]. The ratio of normalized nuclei concentration to the double-averaged concentration is defined as

$$\mathcal{N}_d(\boldsymbol{\xi}, r) = \frac{[\hat{n}(t \rightarrow \infty, \mathbf{x}_{\text{si}}, \mathbf{x}_{\text{so}}, r)]_{d=|\mathbf{x}_{\text{si}}-\mathbf{x}_{\text{so}}|}}{\langle \hat{n} \rangle_{\infty}(r)}, \quad (15)$$

where the variable  $\boldsymbol{\xi}$  represents the different source-sink combinations that are at a distance  $d$ .  $\mathcal{N}_d(\boldsymbol{\xi}, r)$  is a random variable in  $\boldsymbol{\xi}$  and its statistical properties are described in Fig. 4.

Figures 4(A) and 4(B) show iso-surfaces of  $\mathcal{N}_d$  (in green), for two different nuclei sizes for a specific source location within the room. Also presented are spherical surfaces of distance  $d = 2, 4$ , and 8 m. It is clear from the figure that the nuclei concentration can be twice as large as the double-averaged concentration even for the smallest nuclei sizes at a distance of 4 m and below. The higher concentration at smaller separation distances is to be expected and will be compensated by lower than double-averaged concentration for farther separations. This departure from the well-mixed concentration as a function of source-sink separation distance increases with increasing nuclei size. As can be expected, the larger nuclei have a higher probability of being closer to the source than farther away. It is important to note that even the nuclei of radius  $12.5 \mu\text{m}$  have nonnegligible concentrations away from the source, and it is likely that their influence on pathogen concentration may need to be accounted for.

Statistics obtained with all possible source locations are shown in Figs. 4(C)–4(E). The average value  $\langle \mathcal{N}_d \rangle_{\text{so}}$  obtained by averaging over all possible source locations is shown in Fig. 4(C) plotted as a function of  $\tilde{V}_s$  for source-sink separation distances of  $d = 1, 2, 4$ , and 8 m. For small nuclei of size  $\tilde{V}_s \lesssim 1$ ,  $\langle \mathcal{N}_d \rangle_{\text{so}}$  is nearly independent of nuclei size with the concentration being larger than the double-average for  $d \approx 4$ . Larger nuclei segregate into regions of much higher concentration at distances smaller than 2 m and much lower concentration at larger distances.

The value of  $\mathcal{N}_d$  evaluated on a surface separated by a distance  $d$  shows substantial variation which is characterized by the normalized standard deviation  $\sigma_d / \langle \mathcal{N}_d \rangle_{\text{so}}$  shown in Fig. 4(D). For small nuclei of size  $\tilde{V}_s \lesssim 1$ , the standard deviation ranges from 41% of the mean at  $d = 1$  m, to about 10% at  $d = 8$  m. For larger nuclei sizes, the standard deviation is substantially larger indicating the possibility of local source-sink combinations whose probability of viral contagion is far in excess of the well-mixed prediction.

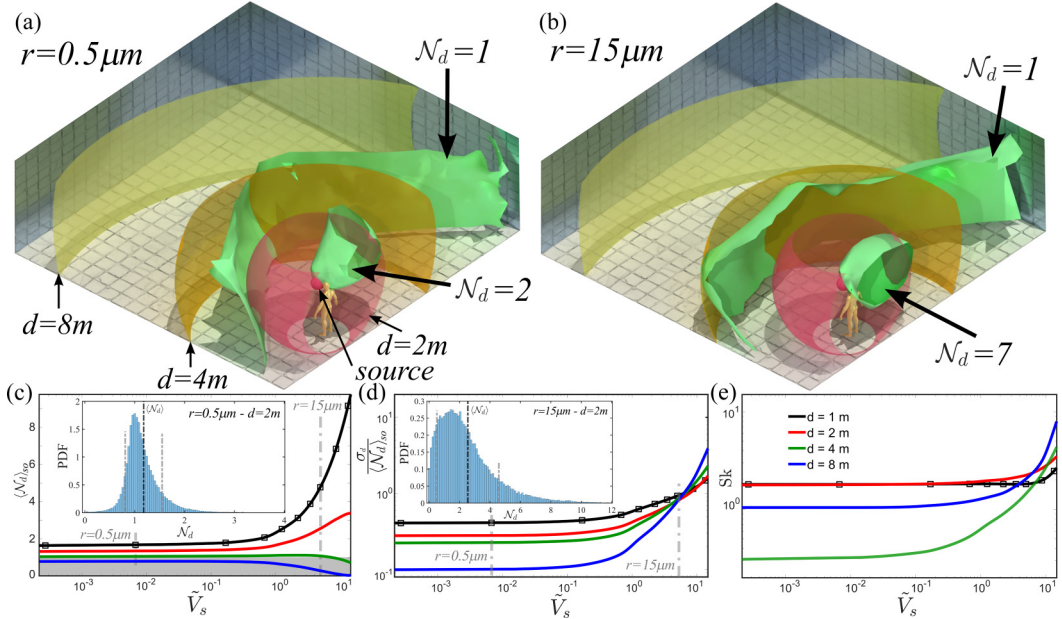


FIG. 4. For the  $ACH = 5$  case, iso-surfaces of normalized concentration shown as green surfaces (A) equal to 1 and 2 times the double-averaged value for  $r = 0.5 \mu\text{m}$  and (B) equal to 1 and 7 times the double-averaged value for  $r = 12.5 \mu\text{m}$ . Also shown are the source location and spherical surfaces of distances  $d = 2, 4,$  and  $8 \text{ m}$ . Panels C, D, and E, show  $\langle \mathcal{N}_d \rangle_{so}$ ,  $\sigma_d / \langle \mathcal{N}_d \rangle_{so}$ , and skewness as a function of normalized settling velocity for four different source-sink separation distances. In panel C, the region of normalized mean value less than 1.0 is shaded light gray. The value above this shaded region indicates pathogen concentration larger than the well-mixed value. Insets in panels C and D show the PDF of  $\mathcal{N}_d$  for (C)  $r = 0.5 \mu\text{m}$  and (D)  $r = 12.5 \mu\text{m}$  at a distance of  $d = 2 \text{ m}$ .

Figure 4(E) shows the skewness plotted as a function of  $\tilde{V}_s$  for the different distances. For small nuclei, the skewness of the distribution is generally small and positive. The magnitude decreases with distance and becomes Gaussian-like for  $d = 4 \text{ m}$  and increases again for larger  $d$ . For larger nuclei, with increasing  $\tilde{V}_s$ , the distributions are highly positively skewed. The PDFs of  $\langle \mathcal{N}_d \rangle_{so}$  are shown as insets of Figs. 4(C) and 4(D), for a few sample cases whose mean, standard deviation, and skewness can be confirmed in Figs. 4(C), 4(D), and 4(E).

The implication of these results on the well-mixed assumption can be discussed with the following example. At a source-sink separation of  $2 \text{ m}$ , the average concentration of small nuclei of size  $\tilde{V}_s \lesssim 1$  is  $1.31$  with a standard deviation of  $0.28$ , which indicates that a good fraction of source-sink pairs that are  $2 \text{ m}$  apart have the nuclei concentration  $1.59$  times higher than the room-averaged concentration. For larger nuclei of  $\tilde{V}_s = 10$ , the mean and standard deviation are  $3.15$  and  $1.2$ , which again highlights the substantial probability of finding source-sink pairs with concentrations as high as  $4.35$  times that of the room average. We should note here that while the curves in Figs. 4(C), 4(D), and 4(E) are shown for the case of  $ACH = 5$ , we again observe similar behavior with the other cases of  $ACH = 2.5$  and  $ACH = 10$ .

### VIII. IMPLICATIONS TO SOCIAL DISTANCING GUIDELINES

Our discussions thus far have been focused on fluid dynamical aspects of how the airborne droplet nuclei spread around the room. To proceed further and evaluate the impact on quantities of ultimate interest such as CET, additional information is needed.

Starting from the work of Wells [40], a number of studies [8,45–48] have systematically included the role of physiological factors (breathing rate and droplet size spectra of typical ejection), epidemiological factors (viral concentration in the ejecta, infectivity, and susceptibility), and other factors (filtration efficiency of masks). In this section, we will consider the prediction of airborne spreading of diseases with the inclusion of the effect of systematic departure from well-mixedness, established in the previous sections. We will fully adopt the detailed physiological and epidemiological framework of Bazant and Bush [8] and only modify the droplet nuclei concentration from the well-mixed value to that measured in the present simulations.

Bazant and Bush [8] presented a simplified model of cumulative exposure time (CET). In present variables, the transient form of this model can be expressed as

$$(N\tau)_{\text{wm}} = \frac{\epsilon}{Q_b^2 p_m^2 C_q s_r \overline{\hat{n}}_{\text{wm}}(\tau)}, \quad (16)$$

where  $N$  is the number of receiving hosts in the room,  $\tau$  is the maximum safe CET for a risk tolerance of  $\epsilon$ , and the subscript “wm” indicates estimation using the well-mixed theory.  $Q_b$  is the breathing rate of the infected person and also the inhalation rate of the receiving host. Here,  $p_m$  is the filtration efficiency of the mask, which was taken to be a constant and to be the same for both the infected and receiving hosts.  $C_q$  is the rate of quanta emitted by the infected person and  $s_r$  is susceptibility or relative transmissibility (see Ref. [8] for details). The normalized nuclei concentration  $\hat{n}_{\text{wm}}$  of the well-mixed model given in Eq. (11) is a function of both the nuclei radius  $r$  and time  $t$ . The overbar accounts for the activity of ejection (breathing, speaking, and singing) by defining the following weighted average

$$\overline{\hat{n}}_{\text{wm}}(\tau) = \frac{\int_0^{r_c} \hat{n}_{\text{wm}}(\tau, r) V(r) Q_b n_{\text{so}}(r) dr}{\int_0^{r_c} V(r) Q_b n_{\text{so}}(r) dr}, \quad (17)$$

where  $n_{\text{so}}(r)$  is the concentration of exhaled nuclei of radius  $r$  that remain airborne. We use the same values of  $n_{\text{so}}(r)$  as Ref. [8]. This value depends on the activity of ejection and is extracted from the experimental measurements of Morawska [71]. Following Ref. [8], we have assumed the viral load per volume at ejection to be independent of droplet size and infectivity to be independent of nuclei size. The upper limit of the integrals is taken to be  $r_c$  as predicted by the well-mixed theory.

The above transient analysis was further simplified by Bazant and Bush [8] by considering the steady-state limit of  $\tau \gg 1/[\lambda_{\text{wm}}(r \rightarrow 0)\mathcal{V}]$ . In the steady limit,  $\hat{n}_{\text{wm}}$  is only a function of  $r$  given by  $1/[\lambda_{\text{wm}}(r)\mathcal{V}]$ . As a result, the weighted average given in Eq. (17) is independent of  $\tau$  and this asymptotic value will be denoted as  $\hat{n}_{\text{wm}\infty}$ . Thus, in the steady limit, the plot of occupancy  $N$  versus safe exposure time  $\tau$  becomes a hyperbola, which for smaller values of  $\tau$  must be appropriately replaced with the transient expression given in Eq. (17).

We reduce the effect of departure from well-mixedness to a single multiplicative *correction factor*  $\gamma$  with the following definition:

$$N\tau = \frac{1}{\gamma} (N\tau)_{\text{wm}}, \quad (18)$$

where the cumulative exposure time  $N\tau$  takes into account the specific location of the source and sink. Although  $N\tau$  can be defined for any specific combination of source-sink locations, of particular interest to social distancing guidelines is the correction factor obtained as a function of source-sink separation distance. Thus, we introduce the following definition of CET as a function of separation distance  $d$ ,

$$N\tau = \frac{\epsilon}{Q_b^2 p_m^2 C_q s_r \langle \hat{n} \rangle_d(\tau)}, \quad (19)$$



where similar to Eq. (17),

$$\overline{\langle \hat{n} \rangle_d(\tau)} = \frac{\int_0^{r_{\text{lim}}} \langle \hat{n} \rangle_d(\tau, r) V(r) Q_b n_{\text{so}}(r) dr}{\int_0^{r_{\text{lim}}} V(r) Q_b n_{\text{so}}(r) dr}. \quad (20)$$

In the above,  $\langle \hat{n} \rangle_d(\tau, r)$  is  $\hat{n}(t = \tau, \mathbf{x}_{\text{si}}, \mathbf{x}_{\text{so}}, r)$  averaged over all possible source-sink combinations that are separated by distance  $d$ .

*The advantage of the correction factor is that it greatly simplifies the complex manner in which the actual room-scale flow departs from the well-mixed theory into a single parameter.* Furthermore, it can be easily applied on top of the well-mixed theory. For instance, in the example of a typical American classroom of size 900 ft<sup>2</sup> with a teacher plus 19 students, for a modest risk of  $\epsilon = 10\%$ , Bazant and Bush [8] estimate the safe exposure time for ACH = 8 to be 7.2 h. With the correction factor, the effect of departure from well-mixedness will be to change the safe exposure time to  $7.2/\gamma$  h. Therefore, with a realistic correction factor corresponding to a typical ventilation system, a safe exposure would be 5.8 h. The correction factor can also be easily used to determine the safe occupancy limit for a fixed duration such as 15 min by simply dividing the well-mixed prediction by the correction factor  $\gamma$ .

As per the above transient analysis, the correction factor  $\gamma$  depends on  $\tau$  (and therefore on  $N$ ). In the steady limit, the correction factor becomes a constant which will be denoted as  $\gamma_{\infty}$ , whose value depends only on three sets of information: (i) fluid mechanical information of room shape, size, and the nature of ventilation, (ii) problem-specific information of where the infected and the receiving hosts are located (this varies from a classroom to a restaurant to a COVID ward in a hospital) and the type of mask (N95, surgical, cloth) they are wearing, if any, and (iii) physiological information through the function  $n_{\text{so}}(r)$ , which measures the volumetric concentration of nuclei of radius  $r$  that remain airborne soon after ejection by the source. Due to the assumption that the viral load and infectivity are independent of nuclei size,  $\gamma$  is independent of epidemiological factors.

The radius of the largest airborne nuclei  $r_{\text{lim}}$  plays an important role in the evaluation of  $\gamma$ . Since departure from well-mixed theory increases with increasing nuclei size, a larger value of  $r_{\text{lim}}$  will result in a somewhat larger value of  $\gamma$ . By balancing the time scale of settling and ventilation, Bazant and Bush [8] defined  $r_c$  and limited normalized settling velocity of airborne nuclei to be  $\tilde{V}_s \leq 1$ . From the LES it is quite clear that even larger nuclei of 10 times the settling velocity can remain airborne. In fact, in the context of Fig. 1, it was earlier shown that  $\langle \langle \hat{n} \rangle \rangle_{\infty} V \sim r$ . Therefore, we adopt a different mechanism for limiting the largest airborne nuclei that was presented in Balachandar *et al.* [6]. The droplets at ejection in the upper respiratory tract are substantially larger than their final airborne nuclei size (droplets are more than an order of magnitude larger than the volume of the desiccated nuclei). Thus, the size of the largest airborne nuclei  $r_{\text{lim}}$  was obtained by balancing evaporation and settling during the early stages when the ejected droplets become evaporated nuclei [6]. A simple fit of their result yields

$$r_{\text{lim}} = 0.0026 k'^{0.22} \psi^{1/3} \quad \text{in m}, \quad (21)$$

where  $k' = 4D \text{Nu} \ln(1 + B)/\rho$  is the effective coefficient of evaporation (in m<sup>2</sup>/s) and  $\psi$  is the fractional volume of the final desiccated nuclei compared to the starting droplet volume. In the expression for  $k'$ ,  $D$  is the diffusion coefficient for water vapor in air, Nu is Nusselt number,  $B$  is Spalding mass number, and  $\rho$  is water-to-air density ratio. As discussed in Ref. [65], ambient temperature and humidity play an important role in determining the value of  $k'$  and  $r_{\text{lim}}$ . With  $k' = 2.135 \times 10^{-8}$  m<sup>2</sup>/s and  $\psi = 0.01$ , which corresponds to an ambient condition of somewhere between dry and humid condition [65], we obtain  $r_{\text{lim}} = 11.5 \mu\text{m}$ .

We shall now evaluate the correction factor for a few different scenarios. First, consider the case of the source and sink being anywhere in the room but separated by a distance  $d$ . Let the infected person be engaged in one of the following expiratory activities: mouth breathing, nose breathing, singing, singing softly, speaking, or whispering. The airborne droplet nuclei size spectra  $[n_{\text{so}}(r)]$  ejected by these activities is reported in Ref. [71] (also see Fig. 1 of Ref. [8]). The steady-state

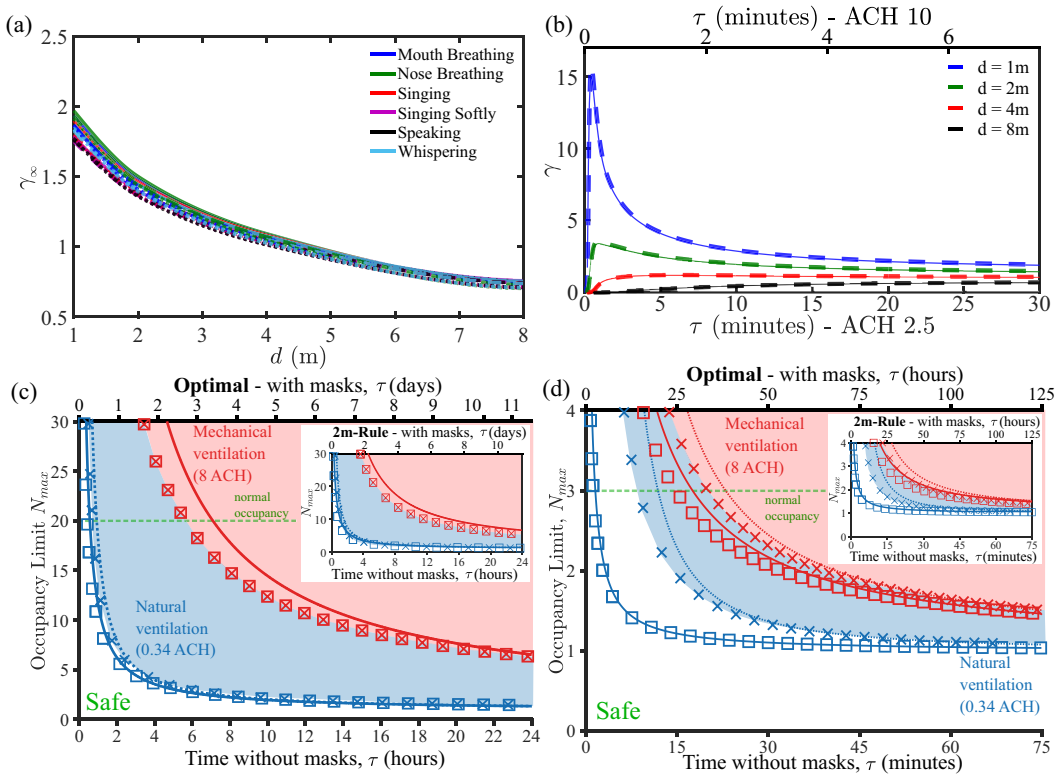


FIG. 5. (A) Steady-state correction factor as a function of source-to-sink distance for different expiratory activities and at different ACH (solid, dashed, and dotted correspond to ACH of 2.5, 5, and 10, respectively). (B) Time-dependent correction factor for ACH 10 (solid) and 2.5 (dashed) as a function of exposure time for distances of  $d = 1$  m (blue), 2 m (green), 4 m (red), and 8 m (black). (C, D) Occupancy vs safe exposure time plots, similar to those present in Bazant and Bush [8]. Their well-mixed results are shown as lines. The present results that account for departure from well-mixedness are in symbols. Red: ACH = 8 and Blue: ACH = 0.34. Solid/square: steady-state analysis; dotted/cross: transient analysis. panel (C) is for the classroom and panel (D) is for the nursing home. The main frames correspond to “optimal” scenario and the inset of the “2-m-rule” scenario.

correction factor  $\gamma_\infty$  computed for these activities plotted as a function of  $d$  for the three different ACH is shown in Fig. 5(A). The colors indicate the different expiratory activities, and the line types of solid, dashed, and dotted correspond to the ACH value of 2.5, 5, and 10, respectively. Most surprisingly,  $\gamma_\infty$  depends primarily on the separation distance  $d$  and does not vary with ejection activity. At distances smaller than 2m, the steady-state correction factor is larger than 1.65 and decreases with increasing distance. The dependence on ACH is weak with a slight reduction with increasing ACH. The steady-state correction factor becomes equal to unity at a distance of about 5 m at the lower ACH, and at a distance of about 4.5 m at the higher ACH. Thus, at source-sink separation distances smaller than about 5 m, the well-mixed theory on average under-estimates the risk of contagion, while for distances larger than about 5 m, the well-mixed theory’s prediction, on average, is overly restrictive.

The time-dependence of the correction factor is plotted in Fig. 5(B) as a function of  $\tau$  for distances between 1 and 8m, for the two different ACH values of 2.5 (dashed) and 10 (solid) and for the activity of mouth breathing. The behavior of  $\gamma$  can be explained from the fact that it is the ratio of weighted nuclei concentration evaluated in the simulation  $\langle \hat{n} \rangle_d$  to that evaluated with

the well-mixed theory  $\overline{\hat{n}}_{\text{wm}}$ . As per the well-mixed theory, irrespective of the distance  $d$ ,  $\overline{\hat{n}}_{\text{wm}}$  will become positive instantly as soon as the source is initiated and will start exponentially approaching the steady-state value. In contrast, in the simulation,  $\langle \hat{n} \rangle_d$  remains zero for some positive time, which corresponds to the time it takes for the nuclei released at the source at  $t = 0$  to reach the sink location. This is why all the curves in Fig. 5(B) start at zero. For small  $d$ ,  $\langle \hat{n} \rangle_d$  rapidly increases toward the steady-state value much faster than the rate predicted by the well-mixed theory, resulting in a sharp peak followed by a slow decay toward the steady-state value that is larger than unity. For larger  $d$ , since  $\gamma_\infty < 1$ , the approach to the steady-state value is monotonic. Therefore, for all ejection activities, at distances shorter than about 2 m, the correction factor is substantially larger at shorter times. In all cases, the steady-state value seems appropriate for  $\tau \gtrsim 15$  min.

The ease of implementation of the correction factor is further demonstrated by revisiting the two examples considered by Bazant and Bush [8]. The first is a typical school classroom of area  $A = 83.6 \text{ m}^2$  and volume  $V = 301 \text{ m}^3$ . Following Ref. [8] we consider natural ventilation of  $\text{ACH} = 0.34$  and mechanical ventilation of  $\text{ACH} = 8$ . In calculating the correction factor, we consider two scenarios: in the optimal scenario, all the occupants are optimally separated and the source-to-sink distance can be evaluated in terms of occupancy as  $d = \sqrt{A/N}$ . In the 2 m-rule scenario, we set  $d = 2 \text{ m}$  in evaluating the correction factor. In this scenario, we assume that the source and sink follow the rule and are separated by only 2 m, even though the room may permit a larger separation. In both scenarios, we use Eq. (18) to evaluate the corrected safety guideline taking into account the correction factor, where we have assumed speaking to be the appropriate mode for a classroom. Following Ref. [8], the calculation uses a transmissibility of 25%, a cloth mask penetration factor of 30%, and a moderate risk tolerance of 10%. The original safety guideline by Ref. [8] and the corrected one for optimal scenario are presented in Fig. 5(C) for both the transient and steady-state analysis. The effect of correction, as can be expected, is to left shift the well-mixed predictions. At large occupancy, the optimal spacing between the occupants decreases, which increases the correction factor. As a result, for  $N = 20$  the safe exposure time decreases by about a factor of 1.65. As occupancy decreases, the optimal  $d$  increases and the correction factor decreases. In fact, in the case of  $\text{ACH} = 0.34$  the corrected curve intersects the well-mixed result at large  $\tau$ . In this classroom example, since  $\tau$  is typically large, the correction factor for both the transient and steady-state analysis are about the same. The inset of Fig. 5(C) shows the results for the 2 m-rule scenario. In this case, the correction factor remains large even as  $N$  decreases to small values and, as a result, the corrected safety guideline will be lower by a constant value of about 1.65.

The second case considered is a nursing home of  $A = 22.3 \text{ m}^2$  and  $V = 53.5 \text{ m}^3$ . Here again, the following values were taken from Ref. [8]: the transmissibility was set at 100%, the mask penetration factor at 10%, and the risk tolerance was lowered to 1%. The original [8] and corrected safety guidelines are presented in Fig. 5(D) for the optimal scenario, with the 2 m-rule scenario presented in the inset. The results of both the transient and steady-state analyses are presented. The effect of applying the correction factor is similar and results in the left-shift of the curves in the case of optimal spacing, and the left-and-down shift of the curves in the case of the 2 m-rule. Since the safe exposure times are shorter for the nursing home, the effect of correctly using the time-dependent analysis is significant. In any case, while the well-mixed theory offers a solid foundation, taking into account the specific details of source-to-sink separation and departure from well-mixedness can be important. For example, in the transient analysis, for a safe exposure time of 15 min, the occupancy limit decreases from two patients to only one, thus changing the safety guideline.

## IX. CONCLUSIONS

We used large eddy simulations with the Euler-Lagrange point-particle approach to assess the appropriateness of the well-mixed theory in predicting the indoor risk of contagion. We consider a canonical room of dimensions  $10 \text{ m} \times 10 \text{ m} \times 3.2 \text{ m}$  with a four-way cassette air conditioning unit positioned at the center of the ceiling. We take advantage of the one-way coupled nature of the problem and statistically overload the room with a total of 20 million droplet nuclei of radii

ranging from 100 nm to 25  $\mu\text{m}$  to obtain well-converged statistics of their dispersion. We assess the well-mixed theory at four different levels: (i) averaged over all possible locations of the source and sink, (ii) for a fixed source, averaged over all possible sink locations within the room, (iii) for a fixed sink, averaged over all possible source locations within the room, and (iv) averaged over all possible source-sink combinations that are 1 m, 2 m, 4 m, or 8 m apart.

We find the well-mixed theory to be appropriate at level (i) when averaged over all possible source and sink locations, with the simulation results differing by only a few percent compared to the well-mixed theory. We do however observe deviations from the well-mixed theory when the source or sink are chosen to be at particular locations within the room. This is especially apparent for larger droplet nuclei. More importantly, we demonstrate that at source-sink separation distances smaller than 5 m, the well-mixed theory on average under-estimates the risk of contagion, while for distances larger than about 5 m, the well-mixed theory's prediction on average is overly restrictive. We propose an easy-to-implement correction factor that can be used to adjust the safe exposure time or the maximum occupancy limit predicted based on the well-mixed theory. We find this correction factor to be largely independent of ACH or expiratory activity (such as breathing, talking, singing, etc.). Another important finding is that we observe an excellent collapse of results across the different ACH simulations. This implies that the results from a simulation with a particular ACH value can be used to accurately predict the results for a different ACH value under otherwise identical conditions.

#### ACKNOWLEDGMENTS

We gratefully acknowledge support from NSF (EAGER Grant No. 2134083), LG Electronics (Grant No. C2021017165), and University of Florida Informatics Institute.

- 
- [1] L. Morawska, Droplet fate in indoor environments, or can we prevent the spread of infection? *Indoor Air* **16**, 335 (2006).
  - [2] F. Yang, A. A. Pahlavan, S. Mendez, M. Abkarian, and H. A. Stone, Towards improved social distancing guidelines: Space and time dependence of virus transmission from speech-driven aerosol transport between two individuals, *Phys. Rev. Fluids* **5**, 122501(R) (2020).
  - [3] Q. Li, X. Guan, P. Wu, X. Wang, L. Zhou, Y. Tong, R. Ren, K. S. Leung, E. H. Lau, J. Y. Wong *et al.*, Early transmission dynamics in Wuhan, China, of novel coronavirus-infected pneumonia, *New Engl. J. Med.* **382**, 1199 (2020).
  - [4] J. A. Lednicky, M. Lauzard, Z. H. Fan, A. Jutla, T. B. Tilly, M. Gangwar, M. Usmani, S. N. Shankar, K. Mohamed, A. Eiguren-Fernandez *et al.*, Viable SARS-CoV-2 in the air of a hospital room with COVID-19 patients, *Int. J. Infect. Dis.* **100**, 476 (2020).
  - [5] L. Morawska and J. Cao, Airborne transmission of SARS-CoV-2: The world should face the reality, *Environ. Int.* **139**, 105730 (2020).
  - [6] S. Balachandar, S. Zaleski, A. Soldati, G. Ahmadi, and L. Bourouiba, Host-to-host airborne transmission as a multiphase flow problem for science-based social distance guidelines, *Int. J. Multiphase Flow* **132**, 103439 (2020).
  - [7] S. Asadi, N. Bouvier, A. S. Wexler, and W. D. Ristenpart, The coronavirus pandemic and aerosols: Does COVID-19 transmit via expiratory particles? *Aerosol Sci. Technol.* **54**, 635 (2020).
  - [8] M. Z. Bazant and J. W. Bush, A guideline to limit indoor airborne transmission of COVID-19, *Proc. Natl. Acad. Sci. USA* **118**, e2018995118 (2020).
  - [9] Z. Chagla, S. Hota, S. Khan, D. Mertz *et al.*, Re: It is time to address airborne transmission of COVID-19, *Clin. Infect. Dis.* **73**, e3981 (2021).
  - [10] J. W. Tang, W. P. Bahnfleth, P. M. Bluyssen, G. Buonanno, J. L. Jimenez, J. Kurnitski, Y. Li, S. Miller, C. Sekhar, L. Morawska *et al.*, Dismantling myths on the airborne transmission of severe acute respiratory syndrome coronavirus (SARS-CoV-2), *J. Hospital Infect.* **111**, 89 (2021).

- [11] L. F. Moriarty, M. M. Plucinski, B. J. Marston, E. V. Kurbatova, B. Knust, E. L. Murray, N. Pesik, D. Rose, D. Fitter, M. Kobayashi *et al.*, Public health responses to COVID-19 outbreaks on cruise ships' worldwide, February–March 2020, *MMWR Morb. Mortal. Wkly. Rep.* **69**, 347 (2020).
- [12] L. Hamner, High SARS-CoV-2 attack rate following exposure at a choir practice's Kagit County, Washington, March 2020, *Morbidity and Mortality Weekly Report* **69** (2020).
- [13] Y. Shen, C. Li, H. Dong, Z. Wang, L. Martinez, Z. Sun, A. Handel, Z. Chen, E. Chen, M. H. Ebell *et al.*, Community outbreak investigation of SARS-CoV-2 transmission among bus riders in Eastern China, *JAMA Int. Med.* **180**, 1665 (2020).
- [14] H. Nishiura, H. Oshitani, T. Kobayashi, T. Saito, T. Sunagawa, T. Matsui, T. Wakita, M. COVID, R. Team, and M. Suzuki, Closed environments facilitate secondary transmission of coronavirus disease 2019 (COVID-19), *MedRxiv* (2020).
- [15] S. L. Miller, W. W. Nazaroff, J. L. Jimenez, A. Boerstra, G. Buonanno, S. J. Dancer, J. Kurnitski, L. C. Marr, L. Morawska, and C. Noakes, Transmission of SARS-CoV-2 by inhalation of respiratory aerosol in the Skagit Valley chorale superspreading event, *Indoor Air* **31**, 314 (2021).
- [16] S. E. Hwang, J. H. Chang, B. Oh, and J. Heo, Possible aerosol transmission of COVID-19 associated with an outbreak in an apartment in Seoul, South Korea, 2020, *Int. J. Infect. Dis.* **104**, 73 (2021).
- [17] E. A. Meyerowitz, A. Richterman, R. T. Gandhi, and P. E. Sax, Transmission of SARS-CoV-2: A review of viral, host, and environmental factors, *Ann. Intern. Med.* **174**, 69 (2021).
- [18] S. P. Domino, A case study on pathogen transport, deposition, evaporation, and transmission: Linking high-fidelity computational fluid dynamics simulations to probability of infection, *Int. J. Comput. Fluid Dynam.* **35**, 743 (2021).
- [19] L. Bourouiba, E. Dehandschoewercker, and J. W. Bush, Violent expiratory events: On coughing and sneezing, *J. Fluid Mech.* **745**, 537 (2014).
- [20] L. Bourouiba, A sneeze, *New Engl. J. Med.* **375**, e15 (2016).
- [21] S. Asadi, A. S. Wexler, C. D. Cappa, S. Barreda, N. M. Bouvier, and W. D. Ristenpart, Aerosol emission and superemission during human speech increase with voice loudness, *Sci. Rep.* **9**, 1 (2019).
- [22] M. Abkarian, S. Mendez, N. Xue, F. Yang, and H. A. Stone, Speech can produce jet-like transport relevant to asymptomatic spreading of virus, *Proc. Natl. Acad. Sci. USA* **117**, 25237 (2020).
- [23] S. Asadi, C. D. Cappa, S. Barreda, A. S. Wexler, N. M. Bouvier, and W. D. Ristenpart, Efficacy of masks and face coverings in controlling outward aerosol particle emission from expiratory activities, *Sci. Rep.* **10**, 1 (2020).
- [24] M. Abkarian and H. A. Stone, Stretching and break-up of saliva filaments during speech: A route for pathogen aerosolization and its potential mitigation, *Phys. Rev. Fluids* **5**, 102301(R) (2020).
- [25] L. Bourouiba, Turbulent gas clouds and respiratory pathogen emissions: Potential implications for reducing transmission of COVID-19, *J. Amer. Med. Assoc.* **323**, 1837 (2020).
- [26] C. S. Ng, K. L. Chong, R. Yang, M. Li, R. Verzicco, and D. Lohse, Growth of respiratory droplets in cold and humid air, *Phys. Rev. Fluids* **6**, 054303 (2021).
- [27] K. L. Chong, C. S. Ng, N. Hori, R. Yang, R. Verzicco, and D. Lohse, Extended Lifetime of Respiratory Droplets in a Turbulent Vapor Puff and its Implications on Airborne Disease Transmission, *Phys. Rev. Lett.* **126**, 034502 (2021).
- [28] R. Mittal, R. Ni, and J.-H. Seo, The flow physics of COVID-19, *J. Fluid Mech.* **894** (2020).
- [29] V. Vuorinen, M. Aarnio, M. Alava, V. Alopaeus, N. Atanasova, M. Auvinen, N. Balasubramanian, H. Bordbar, P. Erästö, R. Grande *et al.*, Modeling aerosol transport and virus exposure with numerical simulations in relation to SARS-CoV-2 transmission by inhalation indoors, *Safety Sci.* **130**, 104866 (2020).
- [30] J. Wang, M. Alipour, G. Soligo, A. Roccon, M. De Paoli, F. Picano, and A. Soldati, Short-range exposure to airborne virus transmission and current guidelines, *Proc. Natl. Acad. Sci. USA* **118**, e2105279118 (2021).
- [31] Z. Peng, W. Bahnfleth, G. Buonanno, S. J. Dancer, J. Kurnitski, Y. Li, M. G. Loomans, L. C. Marr, L. Morawska, W. Nazaroff *et al.*, Practical indicators for risk of airborne transmission in shared indoor environments and their application to COVID-19 outbreaks, *Environ. Sci. Technol.* **56**, 1125 (2022).

- [32] H. Liu, S. He, L. Shen, and J. Hong, Simulation-based study of COVID-19 outbreak associated with air-conditioning in a restaurant, *Phys. Fluids* **33**, 023301 (2021).
- [33] J. Wilson, S. Miller, and D. Mukherjee, A lagrangian approach towards quantitative analysis of flow-mediated infection transmission in indoor spaces with application to SARS-CoV-2, *Int. J. Comput. Fluid Dynam.* **35**, 727 (2021).
- [34] M. Z. Bazant, O. Kodio, A. E. Cohen, K. Khan, Z. Gu, and J. W. Bush, Monitoring carbon dioxide to quantify the risk of indoor airborne transmission of COVID-19, *Flow* **1**, E10 (2021).
- [35] A. Foster and M. Kinzel, Estimating COVID-19 exposure in a classroom setting: A comparison between mathematical and numerical models, *Phys. Fluids* **33**, 021904 (2021).
- [36] P. van den Driessche, Reproduction numbers of infectious disease models, *Infect. Dis. Model.* **2**, 288 (2017).
- [37] Y. Liu, A. A. Gayle, A. Wilder-Smith, and J. Rocklöv, The reproductive number of COVID-19 is higher compared to SARS coronavirus, *J. Travel Med.* **27**, taaa021 (2020).
- [38] L. Ferretti, C. Wymant, M. Kendall, L. Zhao, A. Nurtay, L. Abeler-Dörner, M. Parker, D. Bonsall, and C. Fraser, Quantifying SARS-CoV-2 transmission suggests epidemic control with digital contact tracing, *Science* **368**, abb6936 (2020).
- [39] R. Zhang, Y. Li, A. L. Zhang, Y. Wang, and M. J. Molina, Identifying airborne transmission as the dominant route for the spread of COVID-19, *Proc. Natl. Acad. Sci. USA* **117**, 14857 (2020).
- [40] W. Wells, Airborne contagion and air hygiene: An ecological study of droplet infections, *J. Amer. Med. Assoc.* **159**, 90 (1955).
- [41] E. Riley, G. Murphy, and R. Riley, Airborne spread of measles in a suburban elementary school, *Amer. J. Epidemiol.* **107**, 421 (1978).
- [42] C. Beggs, C. Noakes, P. Sleigh, L. Fletcher, and K. Siddiqi, The transmission of tuberculosis in confined spaces: An analytical review of alternative epidemiological models, *Int. J. Tuberc. Lung Dis.* **7**, 11 (2003).
- [43] S. Rudnick and D. Milton, Risk of indoor airborne infection transmission estimated from carbon dioxide concentration, *Indoor Air* **13**, 237 (2003).
- [44] C.-M. Liao, C.-F. Chang, and H.-M. Liang, A probabilistic transmission dynamic model to assess indoor airborne infection risks, *Risk Anal.* **25**, 1097 (2005).
- [45] M. Nicas, W. W. Nazaroff, and A. Hubbard, Toward understanding the risk of secondary airborne infection: Emission of respirable pathogens, *J. Occup. Environ. Hyg.* **2**, 143 (2005).
- [46] C. Noakes, C. Beggs, P. Sleigh, and K. Kerr, Modelling the transmission of airborne infections in enclosed spaces, *Epidemiol. Infect.* **134**, 1082 (2006).
- [47] G. Buonanno, L. Morawska, and L. Stabile, Quantitative assessment of the risk of airborne transmission of SARS-CoV-2 infection: Prospective and retrospective applications, *Environ. Int.* **145**, 106112 (2020).
- [48] G. Buonanno, L. Stabile, and L. Morawska, Estimation of airborne viral emission: Quanta emission rate of SARS-CoV-2 for infection risk assessment, *Environ. Int.* **141**, 105794 (2020).
- [49] L.-P. Wang and M. R. Maxey, Settling velocity and concentration distribution of heavy particles in homogeneous isotropic turbulence, *J. Fluid Mech.* **256**, 27 (1993).
- [50] S. Balachandar and J. K. Eaton, Turbulent dispersed multiphase flow, *Annu. Rev. Fluid Mech.* **42**, 111 (2010).
- [51] L. Wang and Q. Chen, Analysis on the well-mixing assumptions used in multizone airflow network models, in Proceedings of the 10th International Building Performance Simulation Association Conference and Exhibition (Building Simulation) (IBPSA, 2007), [https://www.aivc.org/sites/default/files/p887\\_final.pdf](https://www.aivc.org/sites/default/files/p887_final.pdf).
- [52] T. Foat, J. Nally, and S. Parker, Investigating a selection of mixing times for transient pollutants in mechanically ventilated, isothermal rooms using automated computational fluid dynamics analysis, *Build. Sci.* **118**, 313 (2017).
- [53] P. Moin, Advances in large eddy simulation methodology for complex flows, *Int. J. Heat Fluid Flow* **23**, 710 (2002).
- [54] S. Balachandar, K. Liu, and M. Lakhote, Self-induced velocity correction for improved drag estimation in Euler–Lagrange point-particle simulations, *J. Comput. Phys.* **376**, 160 (2019).

- [55] M. Germano, U. Piomelli, P. Moin, and W. H. Cabot, A dynamic subgrid-scale eddy viscosity model, *Phys. Fluids* **3**, 1760 (1991).
- [56] D. K. Lilly, A proposed modification of the Germano subgrid-scale closure method, *Phys. Fluids* **4**, 633 (1992).
- [57] J. Pozorski and J.-P. Minier, On the lagrangian turbulent dispersion models based on the Langevin equation, *Int. J. Multiphase Flow* **24**, 913 (1998).
- [58] P. Fede, O. Simonin, P. Villedieu, and K. Squires, Stochastic modeling of the turbulent subgrid fluid velocity along inertial particle trajectories, in *Proceedings of the Summer Program* (Center for Turbulence Research, Stanford, CA, 2006), pp. 247–258.
- [59] K. Liu, P. Huck, A. Aliseda, and S. Balachandar, Investigation of turbulent inflow specification in Euler–Lagrange simulations of mid-field spray, *Phys. Fluids* **33**, 033313 (2021).
- [60] A. Dehbi, Turbulent particle dispersion in arbitrary wall-bounded geometries: A coupled CFD–Langevin-equation based approach, *Int. J. Multiphase Flow* **34**, 819 (2008).
- [61] A. A. Mofakham and G. Ahmadi, Particles dispersion and deposition in inhomogeneous turbulent flows using continuous random walk models, *Phys. Fluids* **31**, 083301 (2019).
- [62] D. C. Haworth and S. B. Pope, A generalized Langevin model for turbulent flows, *Phys. Fluids* **29**, 387 (1986).
- [63] A. Yoshizawa, A statistically derived subgrid model for the large-eddy simulation of turbulence, *Phys. Fluids* **25**, 1532 (1982).
- [64] J. Ferry and S. Balachandar, A fast Eulerian method for disperse two-phase flow, *Int. J. Multiphase Flow* **27**, 1199 (2001).
- [65] K. Liu, M. Allahyari, J. S. Salinas, N. Zgheib, and S. Balachandar, Peering inside a cough or sneeze to explain enhanced airborne transmission under dry weather, *Sci. Rep.* **11**, 1 (2021).
- [66] M. O. Deville, P. F. Fischer, P. F. Fischer, E. Mund *et al.*, *High-order Methods for Incompressible Fluid Flow*, Vol. 9 (Cambridge University Press, Cambridge, UK, 2002).
- [67] D. Zwick and S. Balachandar, A scalable Euler–Lagrange approach for multiphase flow simulation on spectral elements, *Int. J. High Perform. Comput. Appl.* **34**, 316 (2020).
- [68] F. Q. Hu, On absorbing boundary conditions for linearized Euler equations by a perfectly matched layer, *J. Comput. Phys.* **129**, 201 (1996).
- [69] J. L. Santarpia, V. L. Herrera, D. N. Rivera, S. Ratnesar-Shumate, S. P. Reid, D. N. Ackerman, P. W. Denton, J. W. Martens, Y. Fang, N. Conoan *et al.*, The size and culturability of patient-generated SARS-CoV-2 aerosol, *J. Exposure Sci. Environ. Epidemiol.* (2021), doi: [10.1038/s41370-021-00376-8](https://doi.org/10.1038/s41370-021-00376-8).
- [70] P. Fabian, D. Milton, M. Angel, D. Perez, and J. McDevitt, Influenza virus aerosols in human exhaled breath: Particle size, culturability, and effect of surgical masks, *Epidemiology* **22**, S51 (2011).
- [71] L. Morawska, G. Johnson, Z. Ristovski, M. Hargreaves, K. Mengersen, S. Corbett, C. Y. H. Chao, Y. Li, and D. Katoshevski, Size distribution and sites of origin of droplets expelled from the human respiratory tract during expiratory activities, *J. Aerosol Sci.* **40**, 256 (2009).
- [72] The present room-scale LES does not resolve the early jet-scale ejection physics. Thus, the source must be interpreted as post-ejection source, at the point where the room-scale ventilation flow dominates the jet flow. This difference is small in case of breathing or soft speaking. For more intense ejection, one must include the effect of the jet phase with an analysis similar to that given in Eq. (7) of Ref. [8] (2022).